RESEARCH ARTICLE | OCTOBER 29 2025

Evaporation and micro-explosion characteristics of oxymethylene dimethyl ether–diesel binary droplet

S. K. Vankeswaram ; Thanos Megaritis ; Lionel Ganippa

Physics of Fluids 37, 103358 (2025)
https://doi.org/10.1063/5.0290337

Physics of Fluids ARTICLE pubs.aip.org/aip/pof

Evaporation and micro-explosion characteristics of oxymethylene dimethyl ether–diesel binary droplet

Cite as: Phys. Fluids **37**, 103358 (2025); doi: 10.1063/5.0290337
Submitted: 11 July 2025 · Accepted: 12 October 2025 ·
Published Online: 29 October 2025

View Online Export Citation CrossMark

S. K. Vankeswaram,[a] Thanos Megaritis, and Lionel Ganippa

AFFILIATIONS

Department of Mechanical and Aerospace Engineering, Brunel University London, Uxbridge UB8 3PH, United Kingdom

[a]Author to whom correspondence should be addressed: SaiKrishna.Vankeswaram@brunel.ac.uk

ABSTRACT

This study investigates evaporation behavior, puffing, and micro-explosion in droplets of pure diesel, oxymethylene ether (OME1), and diesel/OME1 blends (20%–90% OME1 by volume) using high-speed backlighting imaging. While the 50% OME1 blend exhibits micro-explosions, the 60% and 70% blends show only puffing, and higher or lower OME1 fractions primarily undergo smooth evaporation. The findings indicate that increasing the OME1 concentration accelerates droplet evaporation. Moreover, the evaporation process exhibits universal behavior when droplet lifetimes are scaled by the characteristic evaporation time scale and the binary mixtures show a behavior similar to a homogenous single-component fuel. A modified D^2-law has been proposed to account for binary mixture composition. Morphological observations reveal two dominant pathways: strong micro-explosions, which lead to explosive disintegration and rapid ligament growth, while weak micro-explosions involve mild puffing, and smooth ligament formation culminating in larger droplets. We further analyze this ligament evolution through a breakup regime map, constructed using non-dimensionalized ligament neck diameter, gamma distribution shape parameter, and ligament aspect ratio. Results show a strong correlation between these parameters, indicating a statistical transition in ligament-to-droplet fragmentation modes. An analysis of the dominated time scales shows that strong micro-explosions occur in an inertial-dominated regime, where the ligament stretching time is relatively much shorter than the capillary time scale, while weak micro-explosions occur at relatively higher time scale ratios, suggesting capillary-dominated breakup. The drop size distribution, driven by inertial-dominated regime, is well described by a gamma distribution. These findings enhance our understanding of multicomponent droplet atomization and its relevance to spray-driven combustion.

NOMENCLATURE

Latin symbols

a	Empirical constant
A	Instantaneous projected droplet area (mm^2)
A_0	Initial projected droplet area (mm^2)
b	Exponent or slope
D	Instantaneous droplet diameter (μm)
D_0	Droplet initial diameter (μm)
D_b	Blob circle diameter (μm)
D_d	Secondary droplet diameter (μm)
D_l	Ligament diameter (μm)
K	Evaporation rate constant
L_l	Ligament length (μm)
n	Gamma distribution shape parameter
Γ	Ligament aspect ratio

Greek symbols

α	Thermal diffusivity (m^2/s)
ε_l	Ligament neck thickness (μm)
μ	Dynamic viscosity (Pa s)
ρ	Liquid density (kg/m^3)
σ	Surface tension (N/m)
τ	Droplet lifetime (s)
τ_b	Breakup time scale (s)
τ_c	Capillary time scale (s)
τ_e	Characteristic evaporation time scale (s)

τ_s Ligament stretching time scale (s)
χ OME1 volume fraction in blend

I. INTRODUCTION

Fossil fuels are widely used in heavy-duty compression ignition (CI) engines, and they are known for their higher thermal efficiency but suffer from emissions challenges, particularly particulate matter (PM) and NOx emissions.[1–3] The global initiative toward cleaner and more efficient combustion technologies has led to increased research into alternative fuels that can reduce emissions and improve combustion performance.[4–6] Oxymethylene ethers (OMEs) are a promising class of synthetic fuels and a family of compounds that can be synthesized from biomass. Their high oxygen content offers significant potential to improve engine performance, reduce emissions, and enhance combustion efficiency when blended with diesel fuel.[4–8]

The atomization characteristics of liquid fuel play a critical role in determining the combustion and emission performance of internal combustion engines. A key phenomenon that enhances the breakup and vaporization of fuel droplets is the occurrence of micro-explosion and puffing. These processes arise from the rapid vaporization of lower-boiling-point components within a droplet due to localized heating, leading either to violent fragmentation (micro-explosion) or to the mild ejection of ligaments and small secondary droplets (puffing) caused by vapor bubble growth and rupture inside the parent droplet.[9–11] The micro-explosion causes the parent droplet to fragment into smaller child droplets, enhancing atomization and promoting faster fuel–air mixing, significantly improving the combustion efficiency.[12–14] This phenomenon is particularly prevalent in fuel blends with wider range of boiling fractions, as these higher volatile fractions evaporate more quickly and are more susceptible to rapid internal pressure build-up. Unlike micro-explosion, which causes violent fragmentation and ligament formation, puffing is characterized by less energetic events and the ejection of relatively few smaller daughter droplets. Several studies have explored the events of micro-explosion and puffing in multicomponent fuel blends.[11,15,16]

Water-in-diesel emulsions have been extensively analyzed due to their promise in reducing NOx and particulate emissions. Researchers have reported that the presence of water leads to secondary atomization through micro-explosion, thereby improving fuel–air mixing and combustion efficiency.[17–22] In particular, Melo-Espinosa *et al.*[18] investigated emulsified fuels with varying percentages of water and surfactant ratios, to explore the surfactant concentrations on the emulsion stability, emulsion droplet size, the occurrence of puffing and micro-explosion. Puffing was observed across all emulsions, but full micro-explosions occurred only in those emulsion droplets without surfactants. In parallel, Ismael *et al.*[19] studied the effect of varying injection pressure on emulsion sprays and showed that at higher pressures dispersed water content reduced due to evaporation, this delayed puffing and suppression of micro-explosion. Puffing was observed primarily in droplets larger than 50 μm, and the likelihood of micro-explosion was linked more to internal droplet structure than global structure of spray size. Antonov *et al.*[20] found that micro-explosion dominated the breakup of non-mixed water/fuel droplets at temperatures $\geq$850 °C, while premixed droplets required >1000 °C. Higher temperatures and smaller droplet sizes reduced ignition delay, with composite droplets igniting faster than pure fuels, indicating micro-explosions may aid early ignition under engine conditions. Fedorenko *et al.*[21] extended this understanding through combined experimental and numerical analysis of composite fuel–water droplets using diesel, kerosene, and rapeseed oil. Their study confirmed that onset times for the puffing/micro-explosion decreased with higher ambient temperatures and smaller droplet sizes. While model predictions closely matched experimental results for diesel and kerosene, the onset time for rapeseed oil was overestimated due to its higher viscosity, which affected nucleation and bubble growth rate. Wang *et al.*[22] provided further details on how ambient temperature impacts the internal dynamics of water-diesel emulsion droplets, identified shift in bubble nucleation sites from the droplet center to surface and complex transitions under micro-explosion conditions. Together, these studies demonstrate that micro-explosion behavior in the water-in-fuel emulsion is governed by a complex interplay of composition, injection dynamics, and thermal conditions which are critical considerations for the development of alternative fuel strategies for an efficient combustion.

Similarly, studies on the blends of alcohol–diesel and alcohol–biodiesel highlight how the difference in volatility and blend composition critically influence micro-explosion and puffing behavior. Avulapati *et al.*[9] found that ternary diesel–biodiesel–ethanol blends exhibit micro-explosions when ethanol content ranges from 10% to 40%, while binary blends of biodiesel and ethanol showed only puffing. Avulapati *et al.*[15] further observed two distinct micro-explosion modes in these ternary blends at 500 °C, influenced by droplet phase separation and internal nuclei distribution, with secondary droplets undergoing similar disruptive behavior. Rao *et al.*[23] demonstrated that butanol/Jet A-1 and acetone–butanol–ethanol (ABE)/Jet A-1 blends show puffing at 30% alcohol content and micro-explosions at higher concentrations. The ABE blends had higher micro-explosion probability than butanol blends, suggesting enhanced atomization and combustion efficiency. In a complementary study, Rao *et al.*[24] revealed that bubble rupture depth and ligament morphology in a fuel droplet blend of ABE are shaped by the proportion of volatile alcohol content. Ethanol blends exhibited more irregular vapor–liquid interface instabilities compared to butanol blends, enhancing breakup and atomization. Huang *et al.*[25] investigated biodiesel/n-propanol droplets, showing that micro-explosion intensity increases with both temperature and optimized n-propanol content. A 1:1 biodiesel–n-propanol ratio at 673–773 K yielded maximum disruption and evaporation. Their findings also emphasized the role of oil membrane formation, and superheating of low-boiling components that initiated micro-explosions. Across these studies, common observations include the occurrence of secondary micro-explosions and strong dependencies on droplet composition and ambient temperature. The potential of alcohol blends to enhance atomization and combustion efficiency arises from their ability to promote rapid, disruptive, and dispersed burning, which improves air utilization and leads to shorter combustion durations.

Engine investigations have highlighted the strong potential of OME/diesel blends as alternative fuels. Lumpp *et al.*[26] showed that OMEs can reduce soot emissions by up to 60% while maintaining NO_x levels, while Härtl *et al.*[27] demonstrated that OME1 blends are effective even under high exhaust gas recirculation (EGR) rates. Pastor *et al.*[28] further reported reduced soot formation with higher-chain OMEs, and Saupe and Atzler[29] noted that the high oxygen content of OMEs suppresses soot precursors, particularly under cold-start conditions. More recently, Pèlerin *et al.*[7] confirmed that OME3–6 blends significantly lower particulate emissions while improving ignition

quality. Collectively, these studies establish OMEs as a promising drop in fuel with practical emission benefits, but they also highlight the need to understand the underlying droplet-scale dynamics that govern evaporation and atomization.

However, the specific mechanisms governing micro-explosion and puffing in OME–diesel blends, especially how OME concentration influences internal bubble dynamics, breakup modes, and ignition characteristics are yet to be fully elucidated. A deeper understanding of these behaviors in diesel–OME blends is essential as OME is considered as drop-in fuel for many practical applications. By examining the influence of OME concentration, this study seeks to address a critical knowledge gap and contribute to the understanding of OME–diesel fuel formulations for next-generation combustion systems. Also, understanding the ligament breakup dynamics in OME–diesel droplets is essential, as it directly governs the secondary atomization processes, influencing droplet size distribution, evaporation rates, and ultimately the combustion performance of these alternative fuel blends. This work advances the fundamental understanding of evaporation and ligament breakup dynamics triggered by micro-explosions, emphasizing the relationship between ligament aspect ratio and fragmentation behavior in multicomponent OME1/diesel droplets. Additionally, the resulting secondary droplet size distribution is quantitatively described using a gamma distribution shaped by ligament-mediated breakup processes.

II. EXPERIMENTAL SETUP

The schematic of the experimental setup used for this study is shown in Fig. 1. This setup enables detailed high-speed visualization of droplet breakup dynamics facilitating a comprehensive understanding of the physical processes governing the puffing and micro-explosion behavior of OME1/diesel fuel blends. A continuous light source, positioned behind a diffuser sheet, provides uniform backlighting to enhance the visibility of the droplet during imaging. The droplet is suspended on the junction of a thermocouple wires having a thickness of 76 μm using a Hamilton syringe of capacity 1.5 μl and is positioned using a traverse system at the center of a cylindrical furnace maintained at 500 °C (773 K). The fuel droplet placed on the thermocouple had an approximate diameter of 1.5 mm. Owing to the thermocouple's diameter being less than one-tenth that of the droplet, its role in initiating micro-explosions or puffing phenomena is deemed negligible in the context of the parent droplet's behavior.[9,15,30] The furnace is covered with a quartz windows, allowing optical access for high-speed visualization without influencing the internal thermal environment. The temperature within the furnace is precisely regulated using an external temperature controller to ensure stable and repeatable thermal conditions through the experiment.

Two distinct imaging settings were employed based on the phenomenon of interest. To capture rapid events such as puffing and micro-explosions, images were recorded using a high-speed camera (Photron SA-X2) at a frame rate of 10 000 fps with an exposure time of 10 μs; a set of ten trials was conducted. To monitor relatively slower changes in the projected area of droplets during evaporation, imaging was performed at 500 fps with an exposure time of 15 μs, with a set of three trials conducted. The spatial resolution is 52.3 μm per pixel. The captured images were analyzed using the open-source image analysis software, ImageJ.[31] The binary fuel blends of diesel and OME1 were prepared on a volume basis inside a fumehood cabinet at a room temperature of 20 °C. For example, a 50/50 blend of diesel and OME1 was prepared using 25 ml of OME1 and 25 ml of diesel. The compositions of the various blends used in the current study are presented in Table I. The naming convention indicates, for example, that OME20D80 consists of 20% OME1 and 80% diesel.

The physical properties such as density (ρ), viscosity (μ), and surface tension (σ) of pure OME1 and diesel[4,32,33] are presented in Table II. Although the density and surface tension values of OME1 and diesel are comparable, OME1 exhibits nearly a ninefold difference in boiling point and viscosity compared to diesel. The physical property of the blend was calculated using a linear, volume fraction-weighted average of the component physical properties.

III. RESULTS AND DISCUSSION

The results are organized to capture the key physical phenomena observed in the present study. Section III A presents the morphological evolution of droplets undergoing evaporation, puffing and micro-explosion, followed by a detailed analysis on evaporation and comparison between strong and weak micro-explosion behaviors based on visual breakup features. Section III B examines the formation and fragmentation mechanisms of ligaments generated during micro-explosions, highlighting the breakup pathways and their dependence

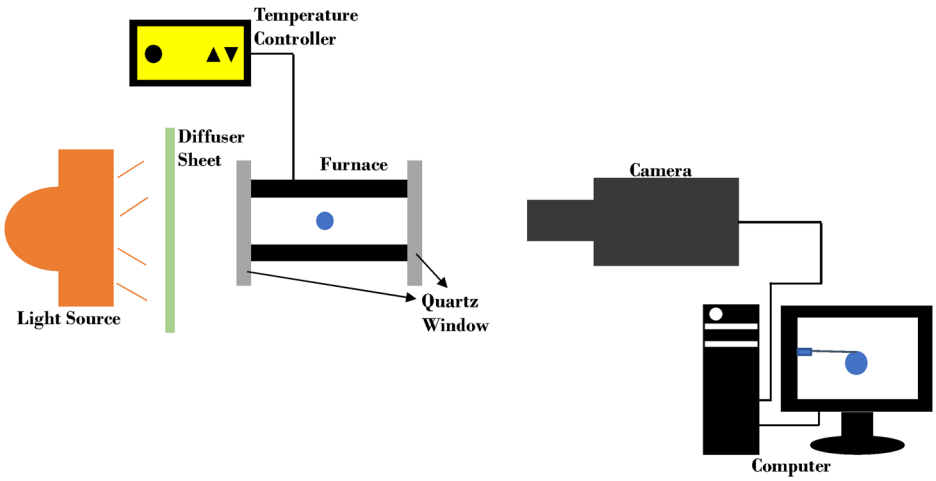

FIG. 1. Experimental setup for high-speed visualization of a single droplet housing on a thermocouple experiencing evaporation, puffing, and micro-explosion inside a furnace.

TABLE I. Composition of various fuel blends used in the present study.

Name	Diesel (%)	OME1 (%)	Fraction of OME1 (χ)
D100	100	0	0.0
OME20D80	80	20	0.2
OME30D70	70	30	0.3
OME40D60	60	40	0.4
OME50D50	50	50	0.5
OME60D40	40	60	0.6
OME70D30	30	70	0.7
OME80D20	20	80	0.8
OME90D10	10	90	0.5
OME100	0	100	1.0

TABLE II. Fuel properties of OME1 and diesel.[4,32,33]

	Boiling point (°C)	Density at 15 °C (Kg/m^3)	Kinematic viscosity at 40 °C (mm^2/s)	Surface tension at 20 °C (mN/m)
Diesel	200–360	839	3.1	28.89
OME1	42	860	0.37	22.81

on internal droplet structure. Finally, Sec. III C provides insights into drop size distribution and analysis of secondary breakup, focusing on the disintegration modes of the ejected fragments.

A. Droplet morphological features

Figure 2 presents the morphological behavior of droplets composed of binary mixtures of OME1 and diesel (denoted by χ, the fraction of OME1) during thermal exposure. For pure diesel ($\chi = 0.0$) and blends with increasing OME1 content up to $\chi = 0.4$, the droplets exhibit simple evaporation without any disruptive phenomena. However, at $\chi = 0.5$ (OME50D50), a distinct micro-explosion event is observed, which is further classified into strong and weak events, reflecting variations in intensity. The phenomenon of micro-explosion is observed in earlier works too at nearly equi-volumetric blends.[15,34] At the highest OME1 concentration ($\chi = 1.0$), pure OME1 again shows simple evaporation which is expected due to lack of volatility contrast. The current trend suggests that a critical balance in volatility and miscibility at $\chi = 0.5$ favors micro-explosion.

The present experiments were carried out across a wide range of blend compositions ($\chi = 0.0$–0.9) to capture the transition in droplet behavior from smooth evaporation to internal boiling leading to puffing and micro-explosion. The results show that disruptive phenomena occur most prominently near the equi-volumetric blend ($\chi \approx 0.5$), where both the volatile (OME1) and less volatile (diesel) components coexist in sufficient quantities to promote internal boiling and heterogeneous vaporization. At intermediate OME1 fractions ($\chi = 0.6$–0.7), only weak puffing events were observed, while at higher OME1 fractions ($\chi \geq 0.8$), evaporation dominated due to the reduced proportion of the less volatile diesel component.

Figure 3 presents a schematic illustration of how blend composition governs the onset of micro-explosions in OME1/diesel binary fuel droplets. The top sequence shows the case of non-equi-volumetric blends, where the volatile component (OME1) is present in relatively small proportion. Upon heating, the small OME1 fraction vaporizes locally within the droplet but lacks the volumetric dominance necessary to accumulate significant internal pressure. As a result, the vapor either diffuses slowly through the diesel matrix or is released via weak bubbling, leading to steady and smooth evaporation without disruptive breakup. In contrast, the bottom sequence represents nearly equi-volumetric blends, where the OME1 content is high enough to saturate the droplet interior. Because OME1 and diesel are nonpolar and therefore fully miscible, disruptive behavior arises primarily from volatility differences rather than phase separation, unlike in immiscible systems (e.g., water–diesel). As heating progresses, OME1 vapor rapidly accumulates, and due to its high volatility and miscibility limits, localized nucleation zones form. These zones cannot dissipate the built-up pressure quickly enough, resulting in a sudden rupture of the droplet interface, a phenomenon recognized as a micro-explosion.[9,11,16] This schematic captures the critical role of blend composition in governing evaporation and secondary atomization dynamics in the current work.

1. Droplet evaporation

The evaporation behavior of different test liquids is explained at first through temporal variation of droplet projected area. Figure 4(a) shows time-dependent variations in the projected area (A/A_0) of fuel droplets for different OME1 fractions, ranging from 0.0 to 1.0 plotted

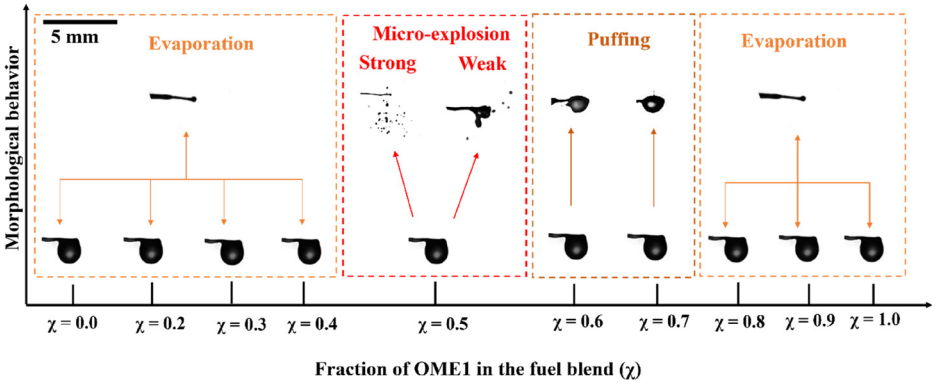

FIG. 2. Morphological behavior of the test liquids. χ is the OME1 fraction in the binary mixture of OME1/diesel.

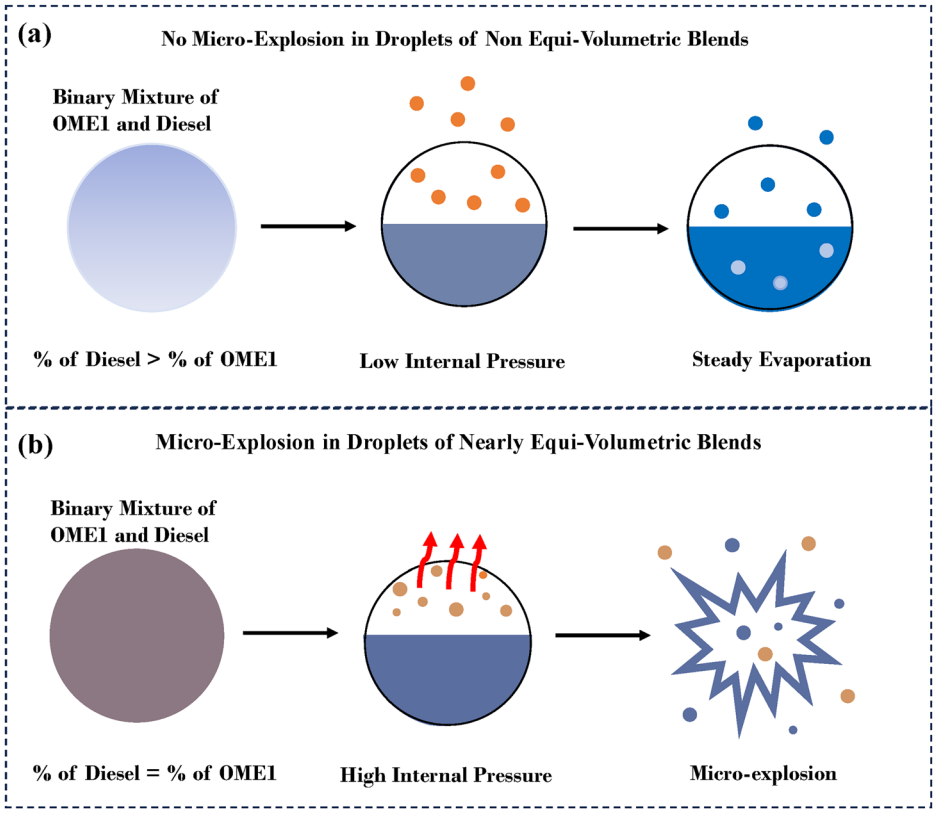

FIG. 3. Conceptual illustration of micro-explosion behavior in OME1(orange)/diesel (blue) droplets based on blend composition. (a) In non-equi-volumetric blends, low OME1 content leads to weak internal vapor pressure and steady evaporation. (b) In nearly equi-volumetric blends, vapor accumulation due to OME1 heating results in high internal pressure and disruptive micro-explosion, producing smaller secondary droplets.

against droplet lifetime, τ. The standard deviation is presented only for $\chi = 0.0$ and $\chi = 1.0$ to maintain clarity and avoid cluttering. The standard deviation for the remaining blends falls within the range of 5%–8%. For all fuel types, A/A_0 decreases over time, indicating droplet evaporation. The pure OME1 ($\chi = 1.0$, brown) decreases the fastest, reaching zero in under 5 seconds owing to its lowest boiling point among the tested fuels (Table II). Blends with more OME1 in diesel ($\chi = 0.9$, $\chi = 0.8$, $\chi = 0.4$, $\chi = 0.3$, and $\chi = 0.2$) show a relatively fast decrease rate compared to pure diesel ($\chi = 0.0$), but slower than pure OME1 ($\chi = 1.0$). The evaporation rate of pure diesel ($\chi = 0.0$, red) decreases the slowest and maintains a larger droplet area for a longer duration. The presence of OME1 enhances evaporation of droplets when blended with diesel. The higher the OME1 content, the faster the droplet evaporation. This could imply better mixing characteristics with increasing OME1 content, which is beneficial for cleaner and more efficient combustion.[4]

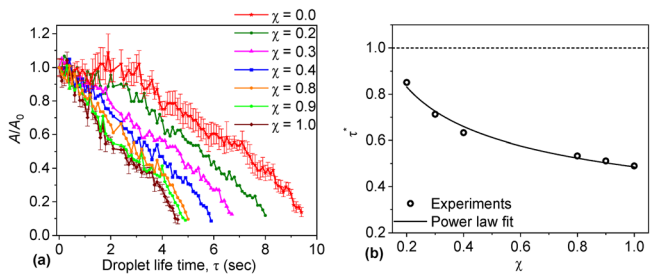

FIG. 4. (a) Time-dependent variations in the projected area of droplets for different OME1 fractions, illustrating how the droplet behavior evolves over the course of the experiment. The standard deviation is presented for $\chi = 0.0$ and $\chi = 1.0$. (b) Variation of non-dimensionalized droplet lifetime during evaporation with the fraction of OME1 (χ) in a fuel blend. A power-law fit is added. The black dotted line indicates the lifetime of the diesel droplet.

The variation of non-dimensionalized droplet lifetime ($\tau^* = \frac{\tau(\chi)}{\tau_{diesel}}$) during evaporation with increasing fraction of OME1 in a fuel blend is presented in Fig. 4(b). The black dotted line represents the baseline lifetime of a pure diesel droplet. As the proportion of OME1 increases, the droplet lifetime decreases in a non-linear fashion, indicating enhanced evaporation rates due to the higher volatility of OME1 compared to diesel. A power law fit is applied to the experimental data to capture this trend for the tested range of χ and for the tested temperature, given as

$$\tau^* = \frac{\tau(\chi)}{\tau_{diesel}} = 0.47\chi^{-0.35}. \quad (1)$$

Figure 5(a) presents the same data as Fig. 4(a) where the droplet lifetime is scaled using the theoretical evaporation time scale (τ_e), which is given by[35,36]

$$\tau_e \propto \frac{D_0^2}{\alpha}, \quad (2)$$

where D_0 is the droplet initial diameter, and α is the thermal diffusivity. The evaporation time scale is interpreted within a conduction-limited framework, as the suspended droplet heats primarily through thermal

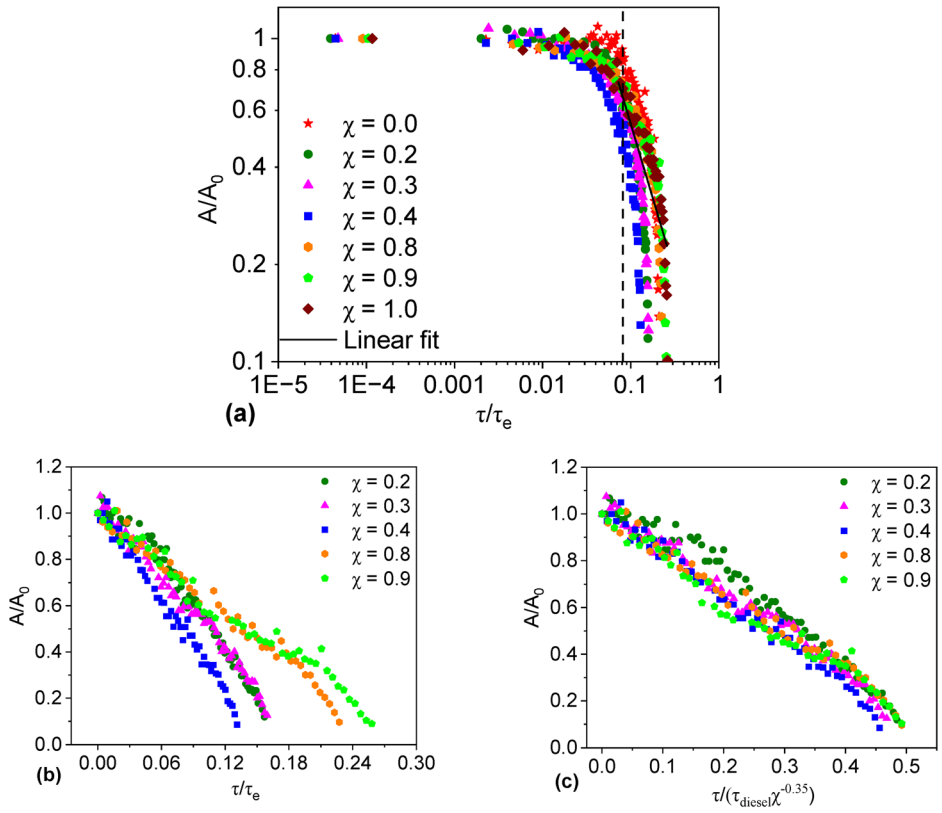

FIG. 5. (a) Variation of droplet projected area plotted against droplet lifetime scaled using evaporation time on a log–log scale. A good collapse of the data are seen using evaporation time scale. Comparison of evaporation behavior across OME1/diesel blends using classical (b) and modified D^2-law time scaling (c).

diffusion from the surface inward. The thermal diffusivity (α) of diesel at 25 °C is reported to be 7.23×10^{-8} m^2/s.[37] Although a direct value for OME1 is not readily available in the literature, we approximated it by using the thermal diffusivity of diethyl ether, which is 1.04×10^{-7} m^2/s at 25 °C, as a close match.[38] Plotted on a log–log scale, the normalized area A/A_0 collapses onto a single curve across all OME1 fractions. This collapse suggests that, despite differences in individual evaporation rates, the process follows a self-similar behavior when appropriately scaled. The analysis confirms the usage of the evaporation time scale in generalizing the evaporation dynamics across different fuel blends, providing a consistent framework for interpreting droplet behavior. The linear trend observed in the log–log plot confirms that A/A_0 and τ/τ_e follow a power law relationship $[\frac{A}{A_0} = a\left(\frac{\tau}{\tau_e}\right)^b]$, with an exponent $b = -0.95$, which agrees well with the classical D^2-law.[35,39] This suggests that the effect of blend composition can be incorporated into the constant ($a = 0.065$), rather than the exponent, b. A ±20% sensitivity analysis on the assumed OME1 thermal diffusivity showed only minor changes in the power-law fit (the exponent varied from −0.95 to −0.90/−0.99, and prefactor from 0.065 to 0.056/0.070), confirming that the proposed scaling is robust to uncertainties in α. The observation that the normalized evaporation curves collapse onto a single trend line across all blend ratios suggests that despite being multicomponent, the droplet evaporation behavior adheres closely to the D^2-law typically reserved for single-component liquids, indicating that the OME1/diesel blends behave quasi-homogeneously under the tested thermal conditions, a finding not previously reported in the literature for such fuel blends.

To account for the influence of fuel composition on evaporation behavior, we propose a modified form of the classical D^2-law tailored for binary OME1/diesel droplets. In the standard model, the droplet diameter squared decreases linearly with time as follows:

$$D^2(\tau) = D_0^2 - K\tau, \tag{3}$$

where K is the evaporation rate constant. The total evaporation time (droplet lifetime) is given by $\tau = \frac{D_0^2}{K}$. It is noted that in the present configuration, the evaporation is not limited by surface kinetics or interfacial energy effects, rather the heating is dominated by bulk conduction, as evidenced by the observed D^2-scaling. However, in multicomponent systems, the effective evaporation rate varies with composition, so the equation for evaporation time becomes

$$\tau(\chi) = \frac{D_0^2}{K(\chi)}. \tag{4}$$

Our experimental data show that the droplet lifetime decreases with increasing χ, following a power-law relationship [Eq. (1)]. Substituting this into the classical D^2-law [Eq. (3)] yields the modified expression

$$\frac{D^2(\tau)}{D_0^2} = 1 - \left(\frac{\tau}{\tau_{diesel}}\right)\chi^{0.35}. \tag{5}$$

The modified D^2-law presented here generalizes the classical single-component droplet evaporation theory to multicomponent fuel systems by embedding blend composition effects directly into the

evaporation time scale. To verify the applicability of the proposed modified D^2-law for multicomponent droplets, the time evolution of normalized droplet area was compared across different OME1/diesel blends using two scaling approaches. In the classical D^2-law, time is normalized by the theoretical evaporation time scale Eq. (2). This method, shown in Fig. 5(b), yielded only partial collapse of the area ratio curves, particularly at higher χ. This deviation can be attributed to two key factors. First, the classical model inherently assumes a single-component droplet and does not account for composition-dependent evaporation dynamics, making it structurally unsuitable for multicomponent systems like OME1/diesel blends. As a result, it cannot capture the shift in evaporation time scale driven by the increasing volatility of OME1. Second, the calculation of the thermal time scale [Eq. (2)] requires accurate thermophysical properties, and uncertainties in parameters like thermal diffusivity of OME1 may further contribute to deviations. In contrast, the modified D^2-law introduced in this work empirically embeds the effect of blend composition through the relation $\tau(\chi) \sim \tau_{diesel} \cdot \chi^{-0.35}$. When this scaling is applied [Fig. 5(c)], evaporation curves for all blends collapse onto a single trajectory, validating the modified law and highlighting its utility in modeling multicomponent droplet evaporation[40,41] where composition influences lifetime, even when the D^2 shape is preserved.

2. Micro-explosion

After the detailed analysis on evaporation in the earlier section, now the attention is directed toward another morphological behavior observed in the present case, which is the micro-explosion at $\chi = 0.5$. Although the concentration and temperature were maintained as constant, the occurrence of micro-explosions was inherently random and chaotic, manifesting as either weak or strong events[15] as highlighted in Fig. 2.

A comparison of both the strong and weak events is presented in Fig. 6, which further illustrates the distinct stages during strong and weak micro-explosions in the OME1/diesel blend with $\chi = 0.5$. In strong micro-explosions, the process evolves through six stages: starting from the initial droplet, followed by internal disruption, bag formation and its breakup, leading to ligament generation and ultimately, secondary droplet formation. In contrast, weak micro-explosions progress through five stages, ending in partial ligament and droplet formation with rebound behavior instead of complete disintegration. This highlights the influence of internal pressure build-up on breakup intensity. Representative high-speed videos of strong and weak micro-explosion events are provided as supplementary material to complement the discussion presented here.

The image sequence given in Fig. 7 captures the complete evolution of a micro-explosion event in a single droplet composed of a 50/50 volumetric blend of OME1 and diesel ($\chi = 0.5$). The sequence begins with the droplet in a stable state (0 ms), followed by the appearance of a tiny surface protrusion at 3.0 ms, indicating the initiation of internal bubble nucleation due to differential volatility between the fuel components. At approximately 5.8–5.9 ms, a sudden micro-explosion occurs, characterized by a violent rupture of the droplet due to a rapid increase in the internal pressure of vapor which leads to an expulsion of a mist from the droplet content outward. This eventually leads to the formation of a bag-like structure composed of liquid sheet with a rim[42] by 6.2 ms, which subsequently fragments into a thin liquid sheet (6.4–7.0 ms), marking the onset of primary ligament formation. As time progresses (8.3–10.9 ms), these primary ligaments undergo stretching, thinning, and break up further into secondary ligaments and satellite droplets, a process driven by inertial and capillary forces. By 12.4 ms, the system exhibits a fully fragmented structure, indicating the culmination of the micro-explosion event and complete disintegration of the parent droplet. This detailed visualization highlights the multistage breakup process and demonstrates the efficiency of OME1/diesel blends in promoting disruptive atomization through micro-explosion mechanisms, which is critical for improving spray dispersion and combustion efficiency in advanced fuel systems.

In micro-explosions, the deformation of drop into a bag-like structure is driven by internal pressure unlike the case of high-speed flows where the external aerodynamic forces cause the deformation.[42] The more volatile OME1 vaporizes rapidly inside the droplet, creating internal pressure that causes the $\chi = 0.5$ droplet outer surface to stretch and deform into a thin membrane, forming a bag-like structure before the droplet ruptures violently.[15,43] The bag is a transient structure formed just before the breakup of the droplet. The Rayleigh–Taylor instability, resulting from the density difference between the OME1 vapor and the liquid diesel phase, plays a significant role in the formation of the bag structure.[44] Additionally, the Kelvin–Helmholtz instability may also contribute to the surface fragmentation of the $\chi = 0.5$ droplet, facilitating the breakup process.[45]

In contrast to the strong micro-explosion behavior presented in Fig. 7, a subsequent observation of a weak micro-explosion in a $\chi = 0.5$ droplet, depicted in Fig. 8, reveals notable differences in breakup

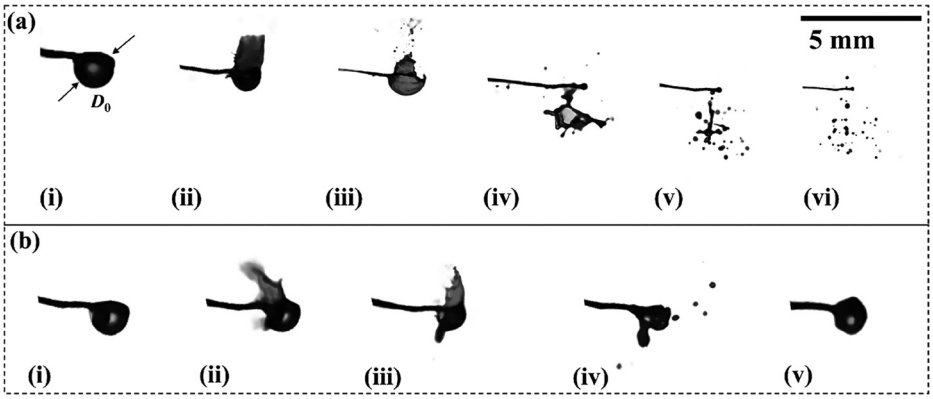

FIG. 6. Comparison of the different stages of strong (a) and weak (b) micro-explosion.

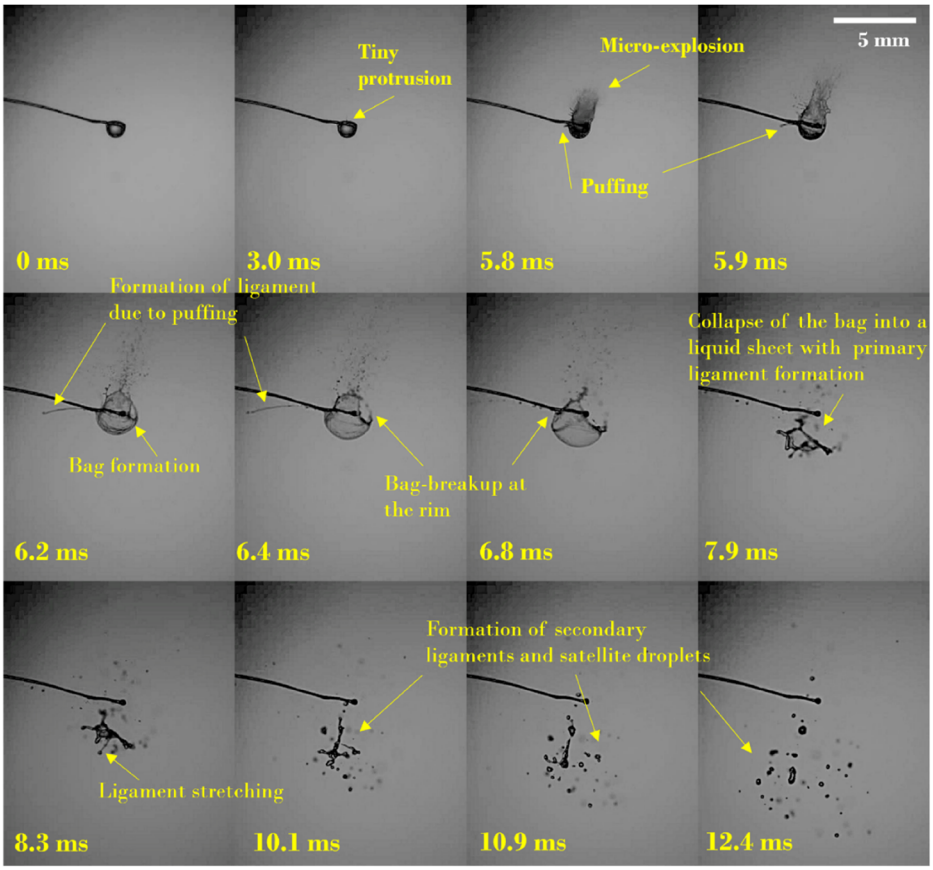

FIG. 7. High-speed imaging sequence showing micro-explosion for $\chi = 0.5$ droplet, illustrating stages from bubble growth to bag rupture, ligament formation, and secondary droplet formation. Multimedia available online.

intensity, morphology, and droplet disintegration dynamics. The image sequence given in Fig. 8 shows a temporal evolution of a weak micro-explosion event observed in a droplet with $\chi = 0.5$. At 0 ms, the droplet remains undisturbed; by 2.2 ms, nucleation begins within the droplet, triggering internal pressure build-up. This is followed by a weak micro-explosion at 2.5 ms, which leads to the formation of a liquid sheet by 2.8 ms. Unlike strong micro-explosions, this event produces smooth ligaments and larger secondary droplets (seen at 3.4–5.2 ms), indicating lower internal pressure and fragmentation energy. By 7.9 ms, a significant portion of the droplet mass remains attached to the thermocouple wires, confirming limited disintegration. Finally, at 12.4 ms, the droplet shows rebound behavior, attributed to surface tension forces overcoming the weak disruptive event. Additionally, the retention of the droplet's bulk on the thermocouple and its subsequent rebound in the weak event further indicate dominance of surface tension over inertial forces, unlike in the stronger case, where inertia drives full disintegration. This sequence underscores the influence of internal nucleation dynamics on breakup morphology and the transition between puffing and micro-explosion regimes.

B. Ligament formation and breakup modes

Further to the comprehension of qualitative droplet morphological behavior, attention is directed to the ligament formation and its

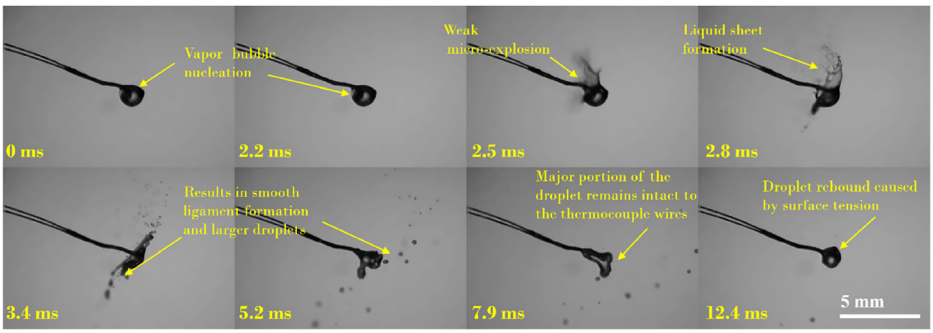

FIG. 8. Temporal sequence illustrating a weak micro-explosion in an $\chi = 0.5$ droplet, showing nucleation, limited sheet formation, and smooth ligament breakup with partial droplet retention. Multimedia available online.

breakup mechanism. Understanding the attributes of these ligaments is crucial in spray dynamics, droplet formation, and combustion processes.[46–48] In combustion systems, the breakup of ligaments significantly influences fuel atomization, droplet size distribution, and consequently combustion efficiency and emissions. For instance, high-velocity airflows can cause ligaments to break up into smaller droplets, enhancing fuel–air mixing and promoting more complete combustion. Conversely, larger droplets may result in incomplete combustion that leads to higher emissions. Therefore, understanding ligament dynamics is crucial for optimizing spray characteristics in various applications, including fuel injection systems and combustion chambers.

Figure 9 illustrates the methodology employed to quantify ligament characteristics during the droplet breakup process. Figure 9(a) shows a high-speed image frame where an individual ligament is identified and selected for further analysis. Figure 9(b) provides a magnified view of this ligament, with specific geometric measurements annotated. The total ligament length, denoted as L_b, is obtained by summing discrete ligament segments $L_{l,1}$, $L_{l,2}$, and $L_{l,3}$, capturing the non-uniform nature of ligament formation and fragmentation. The ligament diameter, D_b, is defined as the mean diameter ($\langle D_b \rangle$) of the blob circle visually highlighted as red-circled regions in Fig. 8. These measurements form the basis for calculating the ligament aspect ratio Γ, which is a key parameter in atomization physics, particularly in understanding how liquid jets or sheets break up into droplets,[47,49] defined as[50]

$$\Gamma = \frac{L_l}{D_l}. \tag{6}$$

Low Γ values correspond to shorter, thicker ligaments which are more likely to break up into smaller number of droplets (may form fewer but larger droplets) via capillary instability. On the other hand, ligaments with high Γ are more likely undergo ligament-mediated breakup which is inertia-driven.[51] The precise spatial quantification shown in Fig. 9 supports the broader objective of correlating ligament morphology with dynamic breakup behaviors and the underlying time scales of the fragmentation mechanisms. The percentage error in L_l varies between 2.3% and 5.16%, while that in D_l ranges from 1.71% to 5.89%. These uncertainties collectively result in a propagated percentage error in Γ between 4.3% and 7.5%. The ligament aspect ratio has a mean of 6.92 with a 95% confidence interval of (5.74, 8.10).

The gamma distribution parameter, n, serves as a statistical indicator of ligament surface behavior in sprays. Higher values of n are associated with smoother ligaments and more uniform breakup, whereas lower n values indicate corrugated ligaments with more irregular and chaotic breakup patterns.[46,47] In the present study, n is determined by measuring the sizes of blobs along the ligaments, as shown in Fig. 9(b), and is expressed as[46,52,53]

$$n = \frac{\langle D_b \rangle^2}{\langle D_b^2 \rangle - \langle D_b \rangle^2}. \tag{7}$$

A detailed analysis of ligament breakup reveals a clear dependency on the ligament aspect ratio Γ. Figure 10 presents a comprehensive analysis of ligament breakup characteristics during droplet disintegration, focusing on the transition between capillary-induced and inertia-driven mechanisms. The ligament aspect ratio serves as a key parameter distinguishing the breakup regimes. In the present case, a critical threshold around $\Gamma \approx 6$ separates the two regimes: Ligaments with $\Gamma < 6$ are predominantly influenced by capillary forces, leading to thicker ligaments and more uniform droplet sizes, as indicated by higher values of the gamma distribution parameter (n) and normalized neck diameters. Conversely, ligaments with $\Gamma > 6$ undergo inertia-driven breakup, characterized by longer, thinner ligaments and a broader droplet size distribution, reflected in lower n values and smaller ε_l/D_0, where ε_l is the neck thickness—the narrowest cross-sectional width of the liquid structure that connects the detaching ligament to the bulk liquid. The accompanying high-speed images [Fig. 10(a)] further support this distinction, illustrating the morphological and statistical differences in ligament evolution and droplet formation based on the governing breakup mechanism. This understanding is crucial for optimizing atomization processes in fuel spray applications, where ligament behavior directly impacts combustion efficiency and emissions.

Further, the ligament breakup behavior was investigated through a time scale analysis by drawing a comparison of two characteristic time scales: the stretching time scale (τ_s) and the capillary time scale (τ_c). The stretching time scale, τ_s, defined as the ratio of the ligament length to its extension rate, characterizes the dominant influence of inertial forces that elongate the ligament,

$$\tau_s = \frac{L_l}{\Delta L_l}\tau_b, \tag{8}$$

where τ_b is the breakup time and ΔL_l is the ligament instantaneous stretching length. In the present work, τ_b is the time interval between

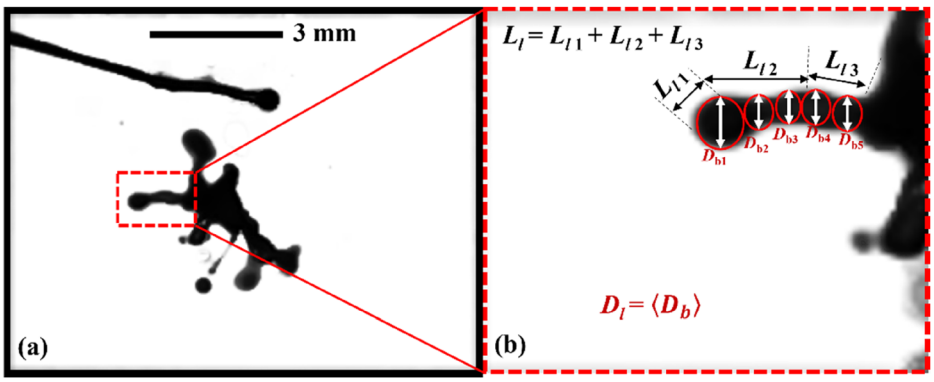

FIG. 9. (a) Representative image showing ligament evolution and measurement geometry. (b) Corresponding magnified view highlighting the region of interest used to extract ligament characteristics.

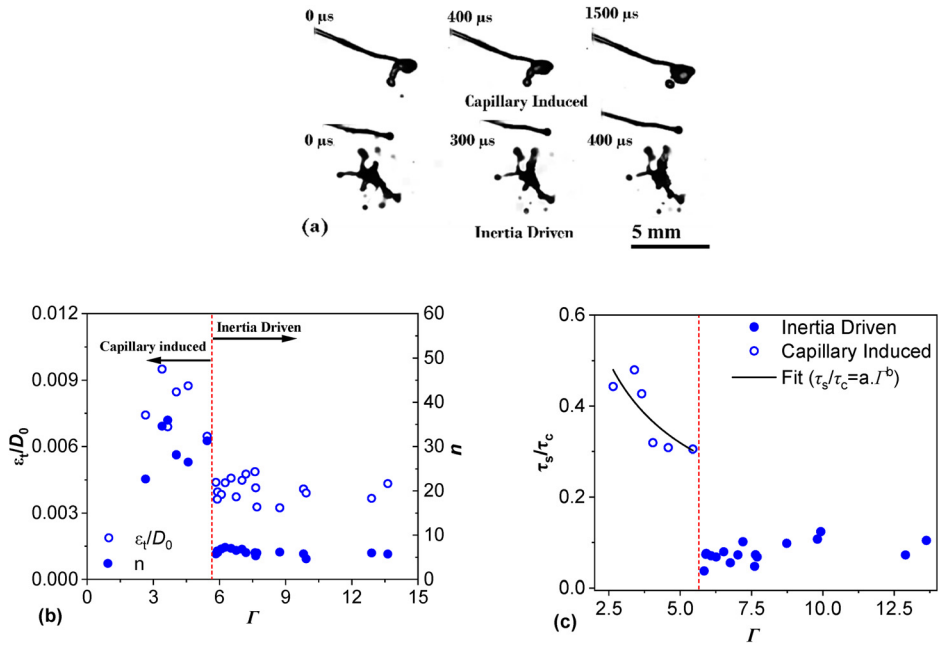

FIG. 10. (a) Image sequence highlighting the different ligament breakup modes, (b) variation of non-dimensional neck diameter and gamma distribution parameter with ligament aspect ratio, and (c) ratio of ligament stretching time scale to capillary time scale plotted against ligament aspect ratio.

the first frame showing the ligament connected to the bulk liquid and the frame where it fully detaches, with no visible connection remaining. In contrast, the capillary time scale, τ_c, determined by the ligament diameter, fluid density, ρ, and surface tension, σ, represents the time required for capillary forces to drive breakup, and is given by[54]

$$\tau_c = \sqrt{\frac{\rho D_l^3}{\sigma}}. \tag{9}$$

By plotting the ratio τ_s/τ_c against the ligament aspect ratio [Fig. 10(c)], a clear transition between two breakup regimes was observed. For Γ values lower than approximately 6, τ_s/τ_c ratios are higher, suggesting capillary forces dominate ligament thinning and breakup (capillary-induced regime). Conversely, for Γ values greater than 6, τ_s/τ_c ratios drop significantly, indicating that inertial forces prevail (inertia-driven regime). This analysis provides a quantitative framework to distinguish between capillary- and inertia-driven ligament breakup modes, and it underpins the observed ligament morphologies in diesel/OME blend during puffing and micro-explosion. The data are fitted using a power-law model with a pre-factor and exponent of 0.616 and −0.402, respectively, for $\Gamma < 6$, showing a clear trend and supporting the inverse relationship between breakup time ratio and ligament aspect ratio.

To provide a physical justification for the observed transition ligament aspect ratio ($\Gamma \approx 6$), we consider a liquid ligament of length "L_l" and diameter "D_l" as shown in Fig. 9. At any intermediate time during stretching, let its length and diameter be $L_{l,0}$ and $D_{l,0}$, respectively. Since the volume is conserved during stretching, assuming the mass fed into the ligament from the bulk liquid to which the ligament is attached is negligible,

$$\pi \frac{D_{l,0}^2}{4} L_{l,0} = C. \tag{10}$$

Differentiating Eq. (10) with respect to time gives a relation between axial stretching and radial contraction rates. After simplification, this reduces to

$$\frac{dD_l}{dt} = -\frac{U_S}{2\Gamma}, \tag{11}$$

where U_s is the stretching velocity of the ligament. Equation (11) can be rearranged to express the characteristics stretching time scale as

$$\tau_S = \frac{2\Gamma D_l}{U_S}. \tag{12}$$

At the threshold between capillary-controlled and inertia-dominated breakup, the stretching and capillary time scales are of the same order: $\tau_c \sim \tau_s$.

Substituting Eq. (12) and capillary time scale Eq. (9) results in a proportional relation, $\frac{D_l}{U_C} \sim \frac{2\Gamma D_l}{U_S}$, where U_c is the capillary velocity given by $U_C = \sqrt{\frac{\rho D_l}{\sigma}}$.

Upon simplification,

$$\Gamma \sim \frac{U_S}{2U_C}. \tag{13}$$

Thus, the ligament aspect ratio at transition is governed by the ratio of stretching to capillary velocities. From the high-speed measurements, the stretching velocity of the ligament was found to be 1.5–2.3 m/s, while the capillary velocity was 0.14–0.25 m/s, giving an average ratio of ∼13. The ligament stretching velocity was obtained using the same displacement-tracking procedure applied earlier for droplet velocities in Fig. 11. This velocity ratio corresponds to ligament aspect ratios in the range of 5–8, consistent with the experimentally observed transition threshold ($\Gamma \approx 6$).

The observed ligament formation and breakup dynamics in OME1/diesel droplets can also be interpreted through the classical

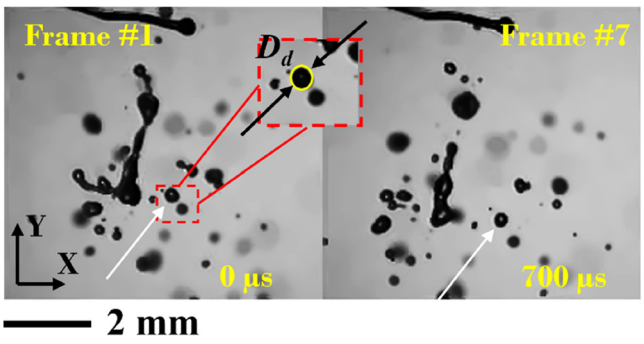

FIG. 11. Image sequence highlighting the measurements of droplet size (D_d) and velocity (U_d).

fluid instability theory and capillary-inertial breakup mechanisms. The transition from weak to strong micro-explosions, characterized by variations in ligament aspect ratio (Γ) and the ratio of stretching to capillary time scales (τ_s/τ_c), aligns with behaviors governed by Rayleigh–Plateau and Rayleigh–Taylor instabilities. Ligaments with lower aspect ratios ($\Gamma < 6$) undergo fragmentation consistent with capillary pinching, where surface tension dominates the breakup process and sets the time scale. In contrast, ligaments with higher aspect ratios ($\Gamma > 6$) display rapid elongation and thinning prior to breakup, indicative of inertia-dominated stretching, similar to mechanisms described in ligament-mediated breakup models. This regime shift is well captured by the time scale ratio τ_s/τ_c, which serves as a useful metric for distinguishing between capillary- and inertia-driven breakup modes. These insights provide a fundamental understanding of ligament dynamics and fragmentation behavior in multicomponent droplets undergoing puffing and micro-explosions.

C. Droplet secondary breakup analysis

A comprehensive examination of ligament properties and their breakup mechanisms naturally extends to the analysis of the resulting droplet characteristics. The droplet size directly affects surface area-to-volume ratio, and the velocity of droplets influences how well they mix with surrounding air or gas, which is essential for flame stability and combustion completeness.[55,56] Figure 11 demonstrates how droplet size and velocity are measured in the present case. The droplet of interest, marked by a yellow circle, exhibited a diameter of 480 μm, measured within a spatial resolution of 52.3 μm. The percentage error involved in the measurement of droplet size ranged from 2.07% to 5.76%. By tracking the droplet's (X, Y) position across consecutive frames (Fig. 11), its instantaneous velocity was computed based on displacement over time. The droplet velocity in the present case ranges from 1.08 to 1.97 m/s for the capillary-induced case and 1.26–4.4 m/s for the inertia-driven case. The results show that capillary-induced breakup produces lower ejection velocities, consistent with surface tension-driven relaxation, while inertia-driven breakup generates significantly higher velocities due to rapid bubble growth and ligament stretching. These measurements provide a complementary quantitative marker of breakup intensity, further distinguishing weak and strong micro-explosions beyond morphological observations.

Research on ligament breakup[46,57] has employed empirical fitting of a single-parameter gamma distribution function to characterize the fragmentation behavior of a corrugated ligament, which is given by

$$P_b\left(n,\ x=\frac{D_d}{\langle D_d\rangle}\right)=\frac{n^n}{\Gamma(n)}x^{n-1}e^{-nx}. \tag{14}$$

The gamma distribution shape parameter value of $n \approx 4$–5 corresponds to highly corrugated ligaments, indicating significant surface undulations during breakup. In contrast, a value of $n=\infty$ represents perfectly smooth ligaments, suggesting minimal perturbation along the ligament interface.[47,52] The experimental probability density function (P_b) is determined based on the droplet count distribution, and is calculated as[58,59]

$$P_b=\frac{N_i}{\Sigma N_i}\left(\frac{\langle D_d\rangle}{\delta D}\right), \tag{15}$$

where N_i is the number of droplets in the i-th size class, δD is the width of the size class, and $\langle D_d\rangle$ represents the average droplet diameter, taken as the arithmetic mean diameter. The value of δD is taken as 100 μm.

Figure 12 presents a comparison between the experimentally obtained probability density function (PDF) of normalized droplet sizes and a theoretical gamma distribution for the inertia-driven regime. The x-axis shows the droplet diameter (D_d) normalized by the mean droplet diameter ($\langle D_d\rangle$), while the y-axis shows the corresponding probability P_b on a logarithmic scale. The experimental data, represented by black circles, follows a characteristic right-skewed shape, indicative of a wide distribution of smaller droplets and fewer large droplets. The solid line corresponds to the gamma distribution, mathematically described by the PDF equation [Eq. (14)], which depends on the shape parameter n [the gamma distribution parameter has a mean of 7.27 with a 95% confidence interval of (6.94, 7.64)] and normalized droplet diameter x. The gamma distribution is able to capture the global experimental trend. Furthermore, the agreement between the experimental data and Eq. (14) suggests that the gamma distribution is a suitable fit for representing the drop size distribution in this breakup

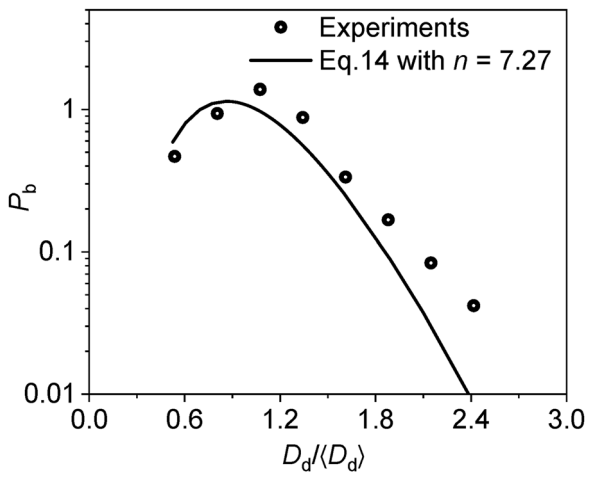

FIG. 12. Comparison of experimental PDF for inertia-driven breakup with gamma distribution given by Eq. (14) with $n=7.27$.

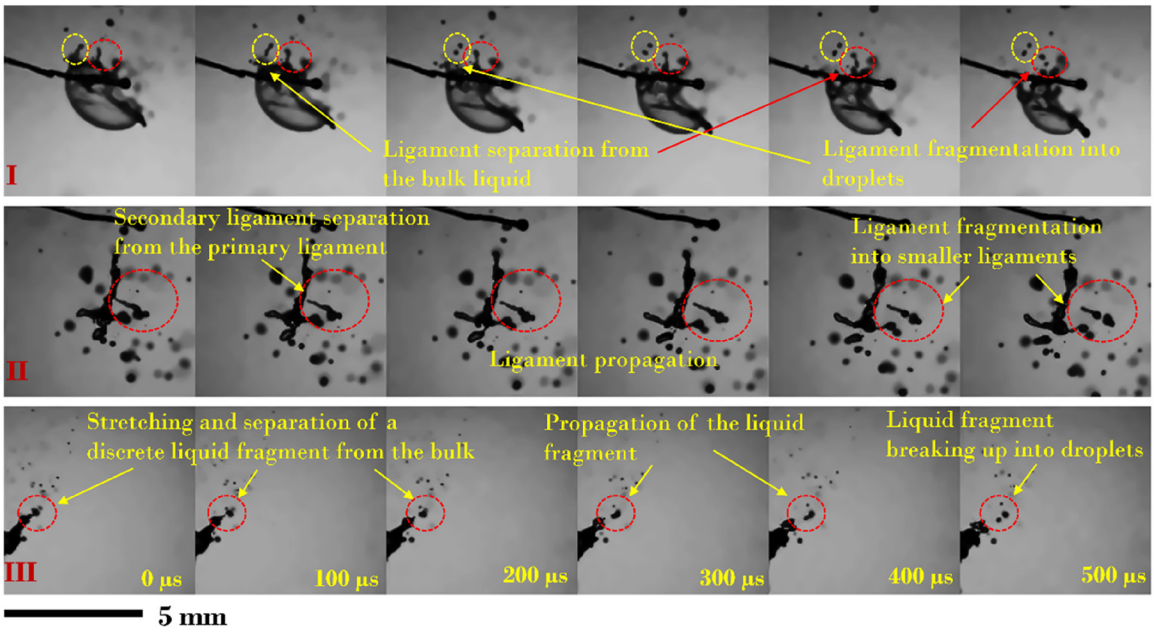

FIG. 13. Sequential imaging of primary and secondary ligament fragmentation, along with discrete droplet disintegration during the micro-explosion of $\chi = 0.5$ droplet, highlighting the various possible breakup mechanisms. The time interval is identical for all three cases shown above.

process. This alignment supports the hypothesis that the droplet formation process is governed by a stochastic fragmentation mechanism, consistent with previous studies on atomization and ligament breakup.[47,52,58]

Figure 13 presents three sequential cases (I, II, and III) illustrating the ligament breakup characteristics during the micro-explosion of $\chi = 0.5$ droplet. In case I, a primary ligament detaches from the bulk liquid and subsequently disintegrates into smaller droplets, highlighting a direct fragmentation pathway. In case II, the breakup is more complex as secondary/tertiary ligaments emerge from the cascading effects of primary breakup, which further divide into smaller structures, representing a hierarchical or multistage breakup mechanism. Case III differs by showing the detachment of a discrete liquid fragment rather than a ligament. Although a few events were observed for this case, this fragment travels forward and then stretches to break up due to capillary effect into multiple satellite droplets. All cases depict high-speed fragmentation dynamics influenced by inertial and surface tension forces, providing a comparative understanding of different breakup modes and their temporal evolution. These observations reveal the structural variations of ligament and droplet formation pathways, depending on the formation of initial ligament geometry and energy conditions. The observed differences (cases I–III) arise from stochastic variations in bubble nucleation and growth rather than compositional effects.[9,15,60] This event-to-event variability is consistent with the weak and strong micro-explosion behavior highlighted earlier in Figs. 6–8, where identical blends exhibit markedly different breakup intensities.

These breakup mechanisms are further characterized using two key geometric metrics: the ligament aspect ratio (Γ) and the droplet-to-ligament diameter ratio (D_d/D_l). Figure 14 highlights distinct trends that differentiate the breakup modes corresponding to the three cases presented in Fig. 13.

- Case I represents ligaments with moderate aspect ratios ($2.5 < \Gamma < 10$), where ligaments undergo intermediate levels of stretching. The resulting droplets are larger than the original ligament diameter (1.22–1.58), indicating a balanced interplay between capillary-driven fragmentation and inertial stretching. This scenario reflects a transitional regime between surface tension-dominated and inertia-influenced breakup.

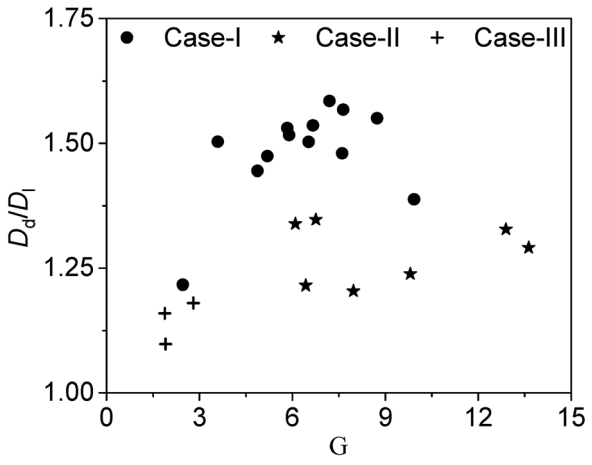

FIG. 14. Ratio of droplet diameter to ligament diameter plotted against ligament aspect ratio for three possible breakup mechanisms shown in Fig. 13.

- Case II corresponds to high aspect ratio ligaments ($\Gamma > 6$), characterized by long, thin structures formed under intense stretching. The primary droplets produced are only slightly larger than the ligament diameter (1.2–1.35), often accompanied by numerous smaller satellite droplets. This suggests a fragmentation process dominated by inertia, where stretching significantly thins the ligament before disintegration.
- Case III involves ligaments with low aspect ratios ($\Gamma < 3$), forming short, thick segments or blob-like structures with minimal elongation. The resulting droplets are approximately equal in size to the ligament diameter (1.1–1.18), indicating a bulk detachment with limited deformation.[24] This reflects an early stage breakup or a regime with low energy input, where surface tension quickly drives the detachment without significant ligament evolution.

These differences directly connect to the parameter correlations shown in Fig. 10(a). In that figure, the gamma distribution shape parameter n was found to increase systematically with ligament aspect ratio Γ. A low value of n, associated with case III (short, thick ligaments), corresponds to a relatively narrow distribution dominated by larger droplets, reflecting an ordered breakup mode governed by capillary pinching. As Γ increases toward the intermediate regime (case I), the shape parameter n also rises, indicating that breakup events become progressively more dispersed and the resulting droplet distribution broadens. At the highest aspect ratios (case II), n reaches its largest values, consistent with a highly polydisperse population produced by inertial stretching and stochastic ligament rupture. Together, these results demonstrate that ligament aspect ratio governs not only the breakup pathway but also the resulting child droplet population, thereby reinforcing the proposed breakup regime map. Among the three identified cases of droplet formation resulting from ligament breakup, it is observed that the highest number of events corresponds to case I, while case III accounts for the fewest occurrences.

IV. CONCLUSIONS

This study presents a detailed investigation into the evaporation and micro-explosion behaviors of pure diesel, pure OME1, and their blends with OME1 fractions ranging from 20% to 90% at an ambient temperature of 500 °C. High-speed backlighting imaging enabled a thorough morphological and quantitative assessment of the droplet breakup processes. The main conclusions are as follows:

- Among the tested blends, the 50% OME1 composition displayed both micro-explosions and puffing, the 60% and 70% blends showed only puffing behavior, whereas higher and lower OME1 fractions exhibited predominantly steady evaporation. Our findings reveal that adding OME1 significantly enhances droplet evaporation rates, with pure OME1 evaporating the fastest and pure diesel the slowest. Additionally, when droplet lifetimes are scaled by the characteristic evaporation time scale, the evaporation behavior appears universal. Under these conditions, the binary mixtures exhibit evaporation characteristics similar to those of a homogeneous single-component fuel. A modified D^2-law has been proposed to account for the blend composition effects.
- Two distinct micro-explosion behaviors were identified. Strong micro-explosions, driven by high internal pressure, lead to violent rupture, fine droplet formation, and high ligament ejection, indicative of an inertia-dominated regime. In contrast, weak micro-explosions are characterized by mild puffing, smooth ligament formation, and the generation of larger droplets, governed primarily by capillary forces.
- Ligament breakup behavior was strongly influenced by the aspect ratio (Γ), with a clear transition observed at $\Gamma \approx 6$. Below this threshold, breakup is capillary-driven, resulting in uniform, thicker ligaments. For $\Gamma > 6$, inertia dominates, producing thinner ligaments and a broader droplet size distribution. This classification was supported by gamma distribution shape parameters and neck diameter analysis.
- A time scale comparison further confirmed this regime distinction. Strong micro-explosions exhibited a much shorter ligament stretching time relative to the capillary breakup time ($\tau_s/\tau_c \ll 1$), while weak events showed relatively higher time scales, reinforcing the influence of inertial and capillary forces, respectively.
- The droplet size distribution for the inertia-driven regime followed a gamma function, indicative of a ligament-mediated breakup.
- Finally, three secondary breakup modes were classified based on ligament geometry: case I with moderate stretching and balanced breakup, case II with long, thin ligaments indicating strong inertial influence, and case III with short, thick ligaments formed under capillary pinching. These findings provide a comprehensive framework for understanding micro-explosion-driven atomization in multicomponent fuel droplets and offer valuable insights for improving combustion efficiency in advanced engine systems.

These insights into evaporation and micro-explosion dynamics of OME1/diesel blends offer practical guidance for optimizing fuel preparation and injection strategies in advanced combustion engines, enabling improved atomization, faster mixing, and potentially lower emissions in real-world application.

V. FUTURE WORKS

Future studies may explore the effects of temperature and initial droplet size in order to estimate shifts in the balance between smooth evaporation and disruptive events.

SUPPLEMENTARY MATERIAL

See the supplementary material for the ImageJ scripts used in data processing and analysis.

ACKNOWLEDGMENTS

We acknowledge the financial support provided by the Engineering and Physical Sciences Research Council (EPSRC), UK, under Grant No. EP/X019578/1. One of the authors, S.K.V., would like to thank Dr. Varun Kulkarni for valuable discussions regarding the manuscript.

AUTHOR DECLARATIONS

Conflict of Interest

The authors have no conflicts to disclose.

Author Contributions

Sai Krishna Vankeswaram: Conceptualization (equal); Data curation (lead); Formal analysis (lead); Software (lead); Writing – original draft (lead); Writing – review & editing (equal). **Thanos Megaritis:** Conceptualization (equal); Funding acquisition (equal); Project administration (equal); Resources (equal); Supervision (equal); Writing – review & editing (equal). **Lionel Ganippa:** Conceptualization (equal); Funding acquisition (equal); Project administration (equal); Resources (equal); Supervision (equal); Writing – review & editing (equal).

DATA AVAILABILITY

The data that support the findings of this study are available from the corresponding author upon reasonable request.

REFERENCES

[1]T. Kamimoto and H. Kobayashi, "Combustion processes in diesel engines," Prog. Energy Combust. Sci. **17**(2), 163–189 (1991).
[2]H. Omidvarborna, A. Kumar, and D.-S. Kim, "Recent studies on soot modeling for diesel combustion," Renewable Sustainable Energy Rev. **48**, 635–647 (2015).
[3]Q. Hu, R. Li, D. Yang, F. Liu, Q. Liu, H. Yue, and Y. Meng, "The evaporation characteristics and molecular cluster variation of diesel droplets in supercritical environment," Phys. Fluids **37**(1), 012115 (2025).
[4]A. Omari, B. Heuser, S. Pischinger, and C. Rüdinger, "Potential of long-chain oxymethylene ether and oxymethylene ether-diesel blends for ultra-low emission engines," Appl. Energy **239**, 1242–1249 (2019).
[5]H. Pitsch, D. Goeb, L. Cai, and W. Willems, "Potential of oxymethylene ethers as renewable diesel substitute," Prog. Energy Combust. Sci. **104**, 101173 (2024).
[6]H. Duan, Q. Song, C. Ren, M. Liu, S. Bai, and G. Li, "Insight into the macroscopic and microscopic characteristics of high-pressure polyoxymethylene dimethyl ethers (PODEn) spray in hydrogen-doped environments," Phys. Fluids **37**(3), 033326 (2025).
[7]D. Pélerin, K. Gaukel, M. Härtl, E. Jacob, and G. Wachtmeister, "Potentials to simplify the engine system using the alternative diesel fuels oxymethylene ether OME1 and OME3 − 6 on a heavy-duty engine," Fuel **259**, 116231 (2020).
[8]F. Mazari, "A study on emission reduction and combustion efficiency, analyzing oxymethylene ether (OME1-5) with diesel fuel," Fuel **375**, 132578 (2024).
[9]M. M. Avulapati, L. C. Ganippa, J. Xia, and A. Megaritis, "Puffing and micro-explosion of diesel–biodiesel–ethanol blends," Fuel **166**, 59–66 (2016).
[10]K. Meng, W. Miao, C. Wang, Z. Huang, X. Zhang, L. Li, and Q. Lin, "Combustion and micro-explosion characteristics of biodiesel–ethanol–aluminum powder particles droplet under simulated air nitrogen–oxygen," Phys. Fluids **35**(10), 102024 (2023).
[11]J. Wang, S. Shi, J. Xu, D. Guan, and Y. Xu, "Micro-explosion and combustion characteristics of multi-component fuel droplet clusters under elevated turbulence intensity," Phys. Fluids **37**(3), 035198 (2025).
[12]C. K. Law, *Combustion Physics* (Cambridge University Press, 2010).
[13]J. Wang, X. Qiao, D. Ju, L. Wang, and C. Sun, "Experimental study on the evaporation and micro-explosion characteristics of nanofuel droplet at dilute concentrations," Energy **183**, 149–159 (2019).
[14]T. Kadota and H. Yamasaki, "Recent advances in the combustion of water fuel emulsion," Prog. Energy Combust. Sci. **28**(5), 385–404 (2002).
[15]M. M. Avulapati, T. Megaritis, J. Xia, and L. Ganippa, "Experimental understanding on the dynamics of micro-explosion and puffing in ternary emulsion droplets," Fuel **239**, 1284–1292 (2019).
[16]D. V. Antonov, P. A. Strizhak, and L. S. Yanovskiy, "Puffing/micro-explosion of two-liquid droplets: Effect of fuel shell composition," Phys. Fluids **36**(6), 062108 (2024).
[17]M. Yahaya Khan, Z. A. Abdul Karim, A. R. A. Aziz, M. R. Heikal, and C. Crua, "Puffing and microexplosion behavior of water in pure diesel emulsion droplets during Leidenfrost effect," Combust. Sci. Technol. **189**(7), 1186–1197 (2017).
[18]E. A. Melo-Espinosa, J. Bellettre, D. Tarlet, A. Montillet, R. Piloto-Rodríguez, and S. Verhelst, "Experimental investigation of emulsified fuels produced with a micro-channel emulsifier: Puffing and micro-explosion analyses," Fuel **219**, 320–330 (2018).
[19]M. A. Ismael, M. R. Heikal, A. R. A. Aziz, C. Crua, M. El-Adawy, Z. Nissar, M. B. Baharom, E. Z. Zainal A, and Firmansyah, "Investigation of puffing and micro-explosion of water-in-diesel emulsion spray using shadow imaging," Energies **11**(9), 2281 (2018).
[20]D. V. Antonov, G. V. Kuznetsov, P. A. Strizhak, O. Rybdylova, and S. S. Sazhin, "Micro-explosion and autoignition of composite fuel/water droplets," Combust. Flame **210**, 479–489 (2019).
[21]R. M. Fedorenko, D. V. Antonov, P. A. Strizhak, and S. S. Sazhin, "Time evolution of composite fuel/water droplet radii before the start of puffing/micro-explosion," Int. J. Heat Mass Transfer **191**, 122838 (2022).
[22]Z. Wang, B. Yuan, J. Cao, Y. Huang, X. Cheng, Y. Wang, X. Zhang, and H. Liu, "A new shift mechanism for micro-explosion of water-diesel emulsion droplets at different ambient temperatures," Appl. Energy **323**, 119448 (2022).
[23]D. C. K. Rao, S. Karmakar, and S. K. Som, "Puffing and micro-explosion behavior in combustion of butanol/Jet A-1 and acetone-butanol-ethanol (ABE)/Jet A-1 fuel droplets," Combust. Sci. Technol. **189**(10), 1796–1812 (2017).
[24]D. C. K. Rao, S. Karmakar, and S. Basu, "Atomization characteristics and instabilities in the combustion of multi-component fuel droplets with high volatility differential," Sci. Rep. **7**(1), 8925 (2017).
[25]X. Huang, J. Wang, Y. Wang, X. Qiao, D. Ju, C. Sun, and Q. Zhang, "Experimental study on evaporation and micro-explosion characteristics of biodiesel/n-propanol blended droplet," Energy **205**, 118031 (2020).
[26]B. Lumpp, D. Rothe, C. Pastötter, R. Lämmermann, and E. Jacob, "Oxymethylene ethers as diesel fuel additives of the future," MTZ Worldwide **72**(3), 34–38 (2011).
[27]M. Härtl, P. Seidenspinner, E. Jacob, and G. Wachtmeister, "Oxygenate screening on a heavy-duty diesel engine and emission characteristics of highly oxygenated oxymethylene ether fuel OME1," Fuel **153**, 328–335 (2015).
[28]J. V. Pastor, A. García, C. Micó, and F. Lewiski, "An optical investigation of Fischer–Tropsch diesel and oxymethylene dimethyl ether impact on combustion process for CI engines," Appl. Energy **260**, 114238 (2020).
[29]C. Saupe and F. Atzler, "Potentials of oxymethylene-dimethyl-ether in diesel engine combustion," Automot. Engine Technol. **7**(3), 331–342 (2022).
[30]H. Ghassemi, S. W. Baek, and Q. S. Khan, "Experimental study on evaporation of kerosene droplets at elevated pressures and temperatures," Combust. Sci. Technol. **178**(9), 1669–1684 (2006).
[31]M. D. Abràmoff, P. J. Magalhães, and S. J. Ram, "Image processing with ImageJ," Biophotonics Int. **11**(7), 36–42 (2004).
[32]F. Wang, J. Wu, and Z. Liu, "Surface tensions of mixtures of diesel oil or gasoline and dimethoxymethane, dimethyl carbonate, or ethanol," Energy Fuels **20**(6), 2471–2474 (2006).
[33]M. Virt and U. Arnold, "Effects of oxymethylene ether in a commercial diesel engine," Cognit. Sustainability **1**(3), 20 (2022).
[34]K. Han, Q. Lin, M. Liu, K. Meng, Z. Ni, Y. Liu, J. Tian, and Z. Qiu, "Experimental study on the micro-explosion characteristics of biodiesel/1-pentanol and biodiesel/methanol blended droplets," Renewable Energy **196**, 261–277 (2022).
[35]F. Dalla Barba, J. Wang, and F. Picano, "Revisiting D2-law for the evaporation of dilute droplets," Phys. Fluids **33**(5), 051701 (2021).
[36]M. A. Saxton, J. P. Whiteley, D. Vella, and J. M. Oliver, "On thin evaporating drops: When is the-law valid?," J. Fluid Mech. **792**, 134–167 (2016).
[37]A. O. Guimarães, F. A. L. Machado, E. C. Da Silva, and A. M. Mansanares, "Investigating thermal properties of biodiesel/diesel mixtures using photopyroelectric technique," Thermochim. Acta **527**, 125–130 (2012).
[38]M. M. Safarov and M. A. Zaripova, "Calculation of the thermal diffusivity of ethers as a function of temperature and pressure," Meas. Tech. **40**(9), 875–878 (1997).
[39]I. Langmuir, "The evaporation of small spheres," Phys. Rev. **12**(5), 368 (1918).
[40]A. Karmakar and S. Acharya, "Numerical simulation of evaporating wavy falling liquid films in laminar gas streams," Int. J. Heat Mass Transfer **198**, 123426 (2022).
[41]C. Albert, H. Marschall, and D. Bothe, "Direct numerical simulation of interfacial mass transfer into falling films," Int. J. Heat Mass Transfer **69**, 343–357 (2014).

[42]L. Opfer, I. V. Roisman, J. Venzmer, M. Klostermann, and C. Tropea, "Droplet-air collision dynamics: Evolution of the film thickness," Phys. Rev. E **89**(1), 013023 (2014).
[43]V. Kulkarni, N. Shirdade, N. Rodrigues, V. Radhakrishna, and P. E. Sojka, "On interdependence of instabilities and average drop sizes in bag breakup," Appl. Phys. Lett. **123**(2), 024101 (2023).
[44]N. Rimbert and G. Castanet, "Crossover between Rayleigh–Taylor instability and turbulent cascading atomization mechanism in the bag-breakup regime," Phys. Rev. E **84**(1), 016318 (2011).
[45]S. T. Thoroddsen, T. G. Etoh, and K. Takehara, "Crown breakup by Marangoni instability," J. Fluid Mech **557**, 63–72 (2006).
[46]P. Marmottant and E. Villermaux, "On spray formation," J. Fluid Mech. **498**, 73–111 (2004).
[47]E. Villermaux, P. Marmottant, and J. Duplat, "Ligament-mediated spray formation," Phys. Rev. Lett. **92**(7), 074501 (2004).
[48]R. Pos, M. Avulapati, R. Wardle, R. Cracknell, T. Megaritis, and L. Ganippa, "Combustion of ligaments and droplets expelled after the end of injection in a multi-hole diesel injector," Fuel **197**, 459–466 (2017).
[49]P. Deepu, S. Basu, and R. Kumar, "Dynamics and fracture of ligaments from a droplet on a vibrating surface," Phys. Fluids **25**(8), 082106 (2013).
[50]K. R. Rajesh, V. Kulkarni, S. K. Vankeswaram, R. Sakthikumar, and S. Deivandren, "Drop size characteristics of sprays emanating from circular and non-circular orifices in the atomization regime," J. Aerosol Sci. **174**, 106245 (2023).
[51]S. Pal, C. Pairetti, M. Crialesi-Esposito, D. Fuster, and S. Zaleski, "Statistics of drops generated from ensembles of randomly corrugated ligaments," Phys. Fluids **36**(11), 112116 (2024).
[52]S. Kooij, R. Sijs, M. M. Denn, E. Villermaux, and D. Bonn, "What determines the drop size in sprays?," Phys. Rev. X **8**(3), 031019 (2018).
[53]S. K. Vankeswaram, M. Maly, and J. Jedelsky, "Understanding the fuel spray characteristics in the near-nozzle region for a pressure swirl atomizer," J. Aerosol Sci. **178**, 106350 (2024).
[54]E. Villermaux, "Fragmentation," Annu. Rev. Fluid Mech. **39**(1), 419–446 (2007).
[55]A. H. Lefebvre and V. G. McDonell, *Atomization and Sprays* (CRC Press, 2017).
[56]N. Sharma, W. D. Bachalo, and A. K. Agarwal, "Spray droplet size distribution and droplet velocity measurements in a firing optical engine," Phys. Fluids **32**(2), 023304 (2020).
[57]I. M. Jackiw and N. Ashgriz, "Prediction of the droplet size distribution in aerodynamic droplet breakup," J. Fluid Mech. **940**, A17 (2022).
[58]S. K. Vankeswaram and S. Deivandren, "Size and velocity characteristics of spray droplets in near-region of liquid film breakup in a swirl atomizer," Exp. Therm. Fluid Sci. **130**, 110505 (2022).
[59]S. K. Vankeswaram, V. Kulkarni, and S. Deivandren, "Spatial evolution of droplet size and velocity characteristics in a swirl spray," Int. J. Multiphase Flow **184**, 105076 (2025).
[60]D. V. Antonov, R. M. Fedorenko, P. A. Strizhak, Z. Nissar, and S. S. Sazhin, "Puffing/micro-explosion in composite fuel/water droplets heated in flames," Combust. Flame **233**, 111599 (2021).